

# Chiral 2D Cu(I) Halide Frameworks

Xiaoqin Ji, Shining Geng, Shuai Zhang, Yaping Gong, Xuanyu Zhang, Ruiqian Li, Yang Liu, Jian Chen, Rui Chen, Zewen Xiao,\* and Lingling Mao\*



Cite This: *Chem. Mater.* 2022, 34, 8262–8270



Read Online

ACCESS |



Metrics & More

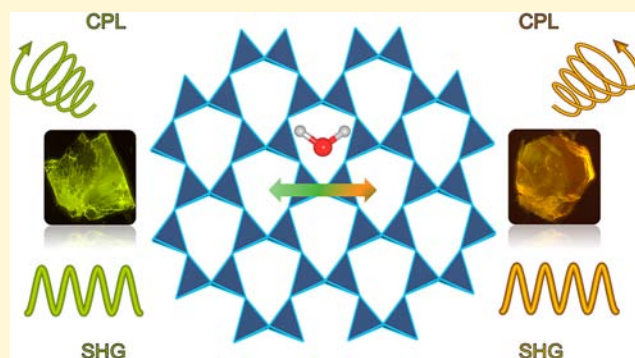


Article Recommendations



Supporting Information

**ABSTRACT:** Hybrid multifunctional materials have great potential in a wide variety of applications due to their flexible combination of organic and inorganic components. Introducing chiral organic modules into the metal halide frameworks can effectively generate multifunctional materials, achieving new functionalities with noncentrosymmetric structures. Here, by incorporating (*R*)- or (*S*)-piperidine-3-carboxylic acid (*R/S*-PCA) as the templating cation, we report the synthesis and characterization of three pairs of new 2D chiral hybrid Cu(I) halides, namely, (*R/S*-PCA)CuBr<sub>2</sub>, (*R/S*-PCA)CuBr<sub>2</sub>·0.5H<sub>2</sub>O, and (*R/S*-PCA)CuI<sub>2</sub>. These chiral Cu(I) halides crystallize in the noncentrosymmetric space group C<sub>2</sub> and belong to a new structural type similar to layered silicates. The optical absorption edges of these chiral materials can be tuned by changing the halide or upon the absorption of water and range from 2.70 to 3.66 eV. A dynamic conversion between (*R/S*-PCA)CuBr<sub>2</sub> and (*R/S*-PCA)CuBr<sub>2</sub>·0.5H<sub>2</sub>O occurs through exposure to moisture or vacuum drying along with changes in the reversible bandgap and photoluminescence. Chiroptical properties such as circular dichroism, circular polarized light emission, and second harmonic generation are investigated. Density functional theory calculations (DFT) show the indirect and direct bandgap natures of these Cu(I) halides and reveal the mechanism for the broadband self-trapped exciton emission at the excited state. The fascinating structural type, chiroptical properties, and reversible hydrochromic behavior of these Cu(I)-based halides make them viable candidates for next-generation multifunctional optoelectronic materials.



## 2 INTRODUCTION

Advanced multifunctional materials that integrate multiple properties in a single crystalline material have attracted a tremendous amount of research interest.<sup>1–7</sup> In recent years, hybrid organic–inorganic metal halides have been considered promising functional materials because of their structural diversity and extraordinary photophysical properties.<sup>8–14</sup> Due to the tunable compositions and flexible crystal structures of hybrid organic–inorganic metal halides, chiral moieties can be rationally introduced into the system as ligands or templating cations, enabling the construction of multifunctional materials.<sup>15–19</sup> Chirality transfer from organic modules to inorganic moieties can be effectively realized not only through the formation of chemical bonds but also through spatial interactions.<sup>20,21</sup> Intrinsic chirality introduced in metal hybrid materials will generally break the symmetry, leading to novel chirality-related optoelectronic properties, such as circular dichroism (CD),<sup>20,22</sup> circularly polarized luminescence (CPL),<sup>23</sup> second harmonic generation (SHG),<sup>24</sup> pyroelectricity,<sup>25</sup> piezoelectricity,<sup>26</sup> and ferroelectricity.<sup>27</sup> In addition, due to the interaction between chirality and spin, the introduction of chirality into organic–inorganic hybrid metal halides with a strong spin orbit coupling system (Pb and I) also has broad application prospects in spintronics.<sup>28,29</sup>

The first study on the chiroptical properties of a hybrid metal halide was performed in 2017,<sup>22</sup> where Moon and co-workers investigated the CD in 2D (*R/S*-MBA)<sub>2</sub>PbI<sub>4</sub> (MBA =  $\alpha$ -methylbenzylammonium). In addition to the extensively studied lead-based chiral metal halides, other materials based on Mn,<sup>30,31</sup> Co,<sup>32</sup> Cd,<sup>33,34</sup> Sn,<sup>18,35</sup> Sb,<sup>36</sup> and Bi<sup>36–38</sup> have also been reported. A series of reports recently demonstrated direct CPL detection using Cu-based chiral metal halides. For instance, Hao et al. demonstrated a direct CPL detector that utilized 0D Cu(II) hybrid chiral semiconductors because of their strong chiroptical activity.<sup>39</sup> Lu et al. also reported 0D chiral hybrid Cu(II) halides that showed the typical spin-polarized charge-transport property.<sup>40</sup> Compared to Cu(II) with a d orbital transition, Cu(I)-based halides with a d<sup>10</sup> closed shell are conducive to achieving a high photoluminescence (PL) efficiency. In particular, Cu(I)-based hybrid halides have the advantages of diverse structural

Received: June 10, 2022

Revised: August 10, 2022

Published: September 2, 2022



tunability and a high photoluminescence quantum yield (PLQY).<sup>41–43</sup> A chiral ligand can be successfully incorporated into the Cu(I) system. For example, Deng et al. synthesized the first example of molecular Cu(I) halides utilizing chiral carbene ligands.<sup>44</sup> Zhang et al. reported a pair of atomically precise copper(I) clusters featuring bright-red luminescence and CPL emission.<sup>45</sup> Wang et al. achieved conspicuously intensified CPL activities in layered-stacking assemblies based on phosphine–copper(I) iodide hybrid clusters.<sup>46</sup> Furthermore, Ge et al. reported two 1D chiral Cu(I) halides that featured highly efficient SHG responses due to structural noncentrosymmetry.<sup>47</sup> Most of the reported Cu(I)-based chiral compounds are coordinated structures with organic ligands, whereas noncoordinated structures with an isolated chiral cation and an anion backbone are reported much less.

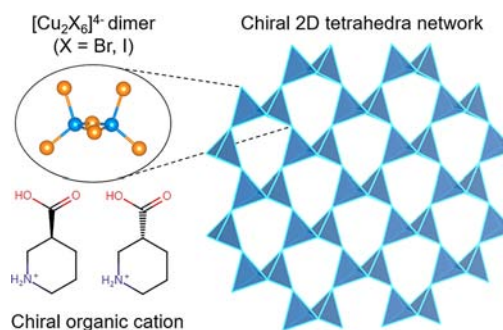
Inspired by the idea of dimensional reduction in a halide perovskite, where larger spacing cations are used to separate the perovskite slabs, an organic cation with appropriate functional groups can be applied in the Cu(I) system to form a layered-framework-type structure. Here, by introducing (*R,S*)-piperidine-3-carboxylic acid (*R,S*-PCA) as the chiral organic templating cation, we report the first examples of chiral Cu(I) halides with cationic and anionic sheets, namely, (*R,S*-PCA)CuBr<sub>2</sub>, (*R,S*-PCA)CuBr<sub>2</sub>·0.5H<sub>2</sub>O, and (*R,S*-PCA)CuI<sub>2</sub>.

The “honeycomb-like” layers are formed due to a special hydrogen bonding interaction between the carboxylate groups and represent a new structural type in the Cu(I)-based halide family. Interestingly, the structures of (*R,S*-PCA)CuBr<sub>2</sub> and (*R,S*-PCA)CuBr<sub>2</sub>·0.5H<sub>2</sub>O can be interconverted by exposure to moisture or vacuum drying and also exhibit reversible PL emissions. Incorporating a chiral cation in these structures leads to their crystallization in the chiral C<sub>2</sub> space group, where their chiroptical properties were investigated. All materials exhibit broad-band CPL emissions at room temperature with decent PLQYs at around 10%. Density functional theory (DFT) calculations reveal the indirect and direct natures of these semiconductors. This new family of chiral Cu(I) halide semiconductors allows us to have a deeper understanding of controlling chiroptical properties with rational structural design.

## 2 RESULTS AND DISCUSSION

**Synthesis and Crystal Structure.** The title compounds were synthesized using stoichiometric amounts of *R,S*-PCA and CuX in HX (X = Br, I) and H<sub>3</sub>PO<sub>2</sub>. Colorless or light yellow plate-like crystals precipitated after the reaction mixture was slowly cooled to ambient temperature. The detailed synthesis conditions are provided in the [Methods section](#). Single-crystal X-ray diffraction revealed that the three hybrid Cu(I) halides all crystallized in the noncentrosymmetric space group C<sub>2</sub>. The crystal structures of all compounds are similar 2D layers and are depicted in [Scheme 1](#) and [Figure 1](#). Detailed crystallographic refinement details are listed in [Tables S1–S3](#). In (*R,S*-PCA)CuBr<sub>2</sub>, 2D layers are formed by [CuBr<sub>4</sub>] tetrahedra connected via corner- and edge-sharing along the *ac*-plane. From the perspective of the *ab*-plane, the 2D network structure is like a twisted honeycomb ([Figure 1d](#)). As depicted in [Figure 1g](#), this new type of 2D structure is due to the significant hydrogen bonds between the carboxylate groups (O···O distance of 2.62 Å) ([Table S4](#)). The protonated *R,S*-PCA moieties are typically located between inorganic layers through O–H···O bonding interactions with the carboxylate groups. In an isolated [CuBr<sub>4</sub>] tetrahedra of (*S*-PCA)CuBr<sub>2</sub>,

**Scheme 1.** Schematic Illustration of the Structural Components in the New Chiral Cu(I)-Based Halide



the Cu–Br lengths are in the range of 2.45–2.53 Å, and the Br–Cu–Br angles range from 101.7° to 116.0°, with a Cu···Cu distance of 2.61 Å ([Table S5](#)). In (*S*-PCA)CuBr<sub>2</sub>·0.5H<sub>2</sub>O, when water molecules are sucked into the structure, the formed honeycomb-like “pores” stretch, and the corresponding average internal angle of the polygon increases from 119.4° to 122.2° ([Figure S2](#)). As shown in [Figure 1f](#), multiple N–H···O and O–H···Br H-bonding interactions are formed between lattice water molecules and amine groups from organic cations (N···O distance of 2.83 Å) and coordinated bromine ions (O···Br distance of 3.28 Å, [Table S4](#)). Compared with that in (*S*-PCA)CuBr<sub>2</sub>, the bond length of the Cu–Br bond increases and falls within a range of 2.49–2.56 Å. The Br–Cu–Br angle changes from 103.4° to 117.3°, with a longer Cu···Cu distance of 2.65 Å ([Table S6](#)). When the halogen is changed from bromine to iodine, a similar 2D layered Cu(I)-based iodide is constructed under similar conditions. Since the electronegativity of iodine is weaker than that of the bromine atom, the formed Cu–I distance is significantly longer, with Cu–I distances of 2.61–2.72 Å, a wider I–Cu–I angle of 100.9°–120.8°, and a shorter Cu···Cu distance of 2.59 Å ([Table S7](#)). However, for Cu(I)-based iodides, water molecules were not observed to adsorb into the structure because the electronegativity of iodine is weaker than that of bromine, making it less attractive for water to be trapped.

**Optical Properties.** The optical bandgaps of these chiral Cu(I)-based halides were determined by diffuse reflectance spectroscopy measurements on solid powder samples ([Figure 3](#)). The optical bandgaps were estimated by extrapolating the absorbing edge to the linear part and follow the order of (*S*-PCA)CuI<sub>2</sub> (2.70 eV), (*S*-PCA)CuBr<sub>2</sub> (2.87 eV), and (*S*-PCA)CuBr<sub>2</sub>·0.5H<sub>2</sub>O (3.66 eV). These bandgaps are comparable with other Cu(I) halides, such as [Me-Py]CuI<sub>2</sub> (2.80 eV),<sup>48</sup> [H<sub>2</sub>DABCO]Cu<sub>3</sub>Br<sub>5</sub> (3.44 eV),<sup>48</sup> and (*R*-MBA)CuBr<sub>2</sub> (4.10 eV).<sup>47</sup> Among these compounds, (*S*-PCA)CuI<sub>2</sub> has the smallest optical bandgap, with a corresponding light yellow color.<sup>36,49</sup> Moreover, in the Cu(I)-based bromides, as more water is absorbed into the framework, the Cu–Br–Cu angle in the honeycomb-like “pores” drastically increases from 147° to 170° ([Figure S2](#)), leading to a significant optical bandgap shift (–0.8 eV). This is consistent with what is shown in [Figure S3](#), where the optical absorption edge gradually blue-shifts. After several checkpoints, the transition was finally complete. Overall, the optical bandgaps here are more affected by the Cu–X–Cu angles (147° for Br, 148° for I, and 170° for the one with water) than the effect of the halide.

Time-resolved PL measurements give averaged decay lifetime for these halides, from the longest of 123.9 μs for



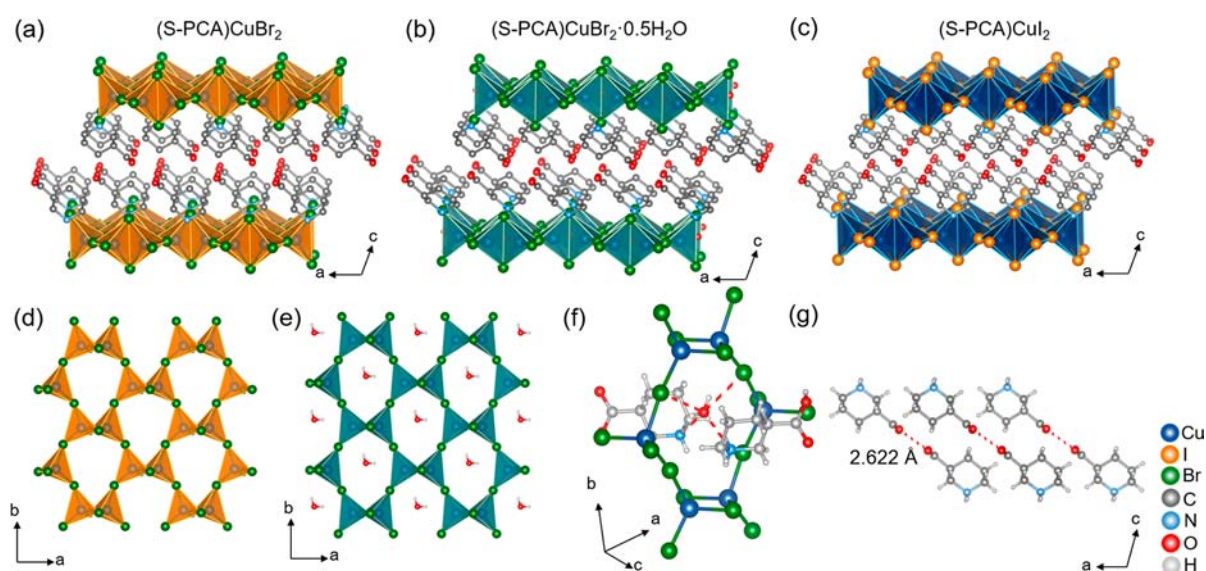


**Figure 1.** Crystal structures of (a) (S-PCA)CuBr<sub>2</sub>, (b) (S-PCA)CuBr<sub>2</sub>·0.5H<sub>2</sub>O, and (c) (S-PCA)CuI<sub>2</sub> as viewed from the *b*-axis. Layered inorganic frameworks of (d) (S-PCA)CuBr<sub>2</sub> and (e) (S-PCA)CuBr<sub>2</sub>·0.5H<sub>2</sub>O as viewed from the *c*-axis. (f) H-bonding interactions (in red dashes) in (S-PCA)CuBr<sub>2</sub>·0.5H<sub>2</sub>O. (g) H-bonding interactions (in red dashes) between carboxyl groups of the organic cations as viewed from the *b*-axis.

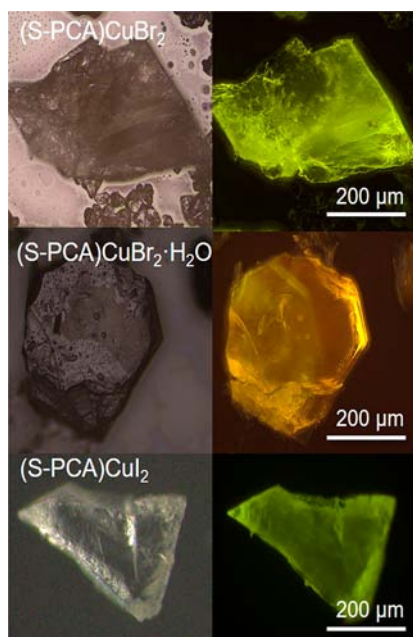


**Figure 2.** Optical microscopic pictures of the three new compounds reported here. The right side shows the PL emission colors of the crystals under LV excitation.

(S-PCA)CuBr<sub>2</sub> to 62.4 μs for (S-PCA)CuBr<sub>2</sub>·0.5H<sub>2</sub>O and the shortest of 4.3 μs for (S-PCA)CuI<sub>2</sub> (Figure 4a). The PLQYs of the three chiral Cu(I)-based halides are 7.5% for (S-PCA)CuBr<sub>2</sub>, 0.5% for (S-PCA)CuBr<sub>2</sub>·0.5H<sub>2</sub>O, and 12.8% for (S-PCA)CuI<sub>2</sub> (see Table 1). This suggests as the water was absorbed, the PL was simultaneously quenched. Compared with the Cu(I)-based bromines, iodide has the highest PLQY and the shortest decay lifetime, which could be related to the iodide-enhanced spin-orbit coupling effect and promoted singlet-to-triplet intersystem crossing.<sup>50,51</sup> Steady-state PL measurements were also performed at room temperature, as shown in Figure 4b and c. All compounds exhibit significant PL emission. As shown in Figure 2, (R,S-PCA)CuBr<sub>2</sub> and (R,S-

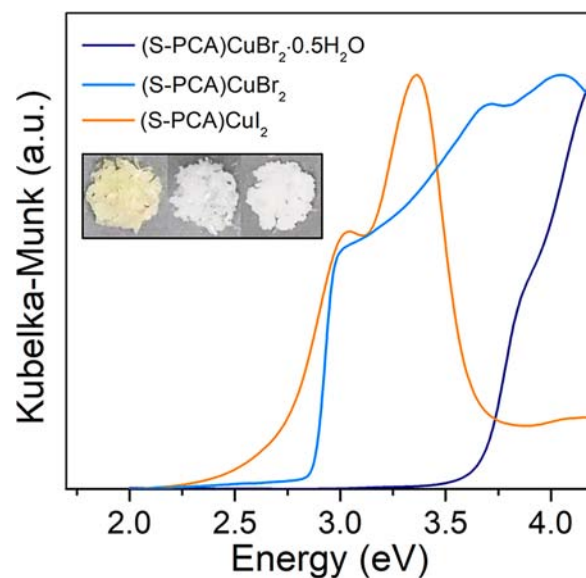


**Figure 3.** UV-vis absorption spectra of (S-PCA)CuI<sub>2</sub>, (S-PCA)CuBr<sub>2</sub>, and (S-PCA)CuBr<sub>2</sub>·0.5H<sub>2</sub>O. The pictures of the powdered samples show their corresponding colors (insert, left to right: (S-PCA)CuI<sub>2</sub>, (S-PCA)CuBr<sub>2</sub>, and (S-PCA)CuBr<sub>2</sub>·0.5H<sub>2</sub>O).

(R,S-PCA)CuI<sub>2</sub> have similar yellow emissions, while (R,S-PCA)CuBr<sub>2</sub>·0.5H<sub>2</sub>O has a significantly different orange emission. The broadband emission spectra with a single peak at around 558 nm (2.22 eV) has a wide full-width at half-maximum (fwhm) of 115 nm for both (R,S-PCA)CuBr<sub>2</sub> and (R,S-PCA)CuI<sub>2</sub>. For (R,S-PCA)CuBr<sub>2</sub>·0.5H<sub>2</sub>O, the emission spectrum is progressively red-shifted from 558 (2.22 eV) to 590 nm (2.10 eV), with a slightly reduced fwhm of 111 nm. All compounds show large Stokes shifts of 231 nm for (R,S-PCA)CuBr<sub>2</sub>, 270 nm for (R,S-PCA)CuBr<sub>2</sub>·0.5H<sub>2</sub>O, and 232 nm for (R,S-PCA)CuI<sub>2</sub>, which are similar to those of many previously reported Cu(I)-based halides.<sup>48</sup> Considering that the Cu...Cu distances of these halides are all less than the sum of van der Waals radius of Cu atoms (2.8 Å), the emission

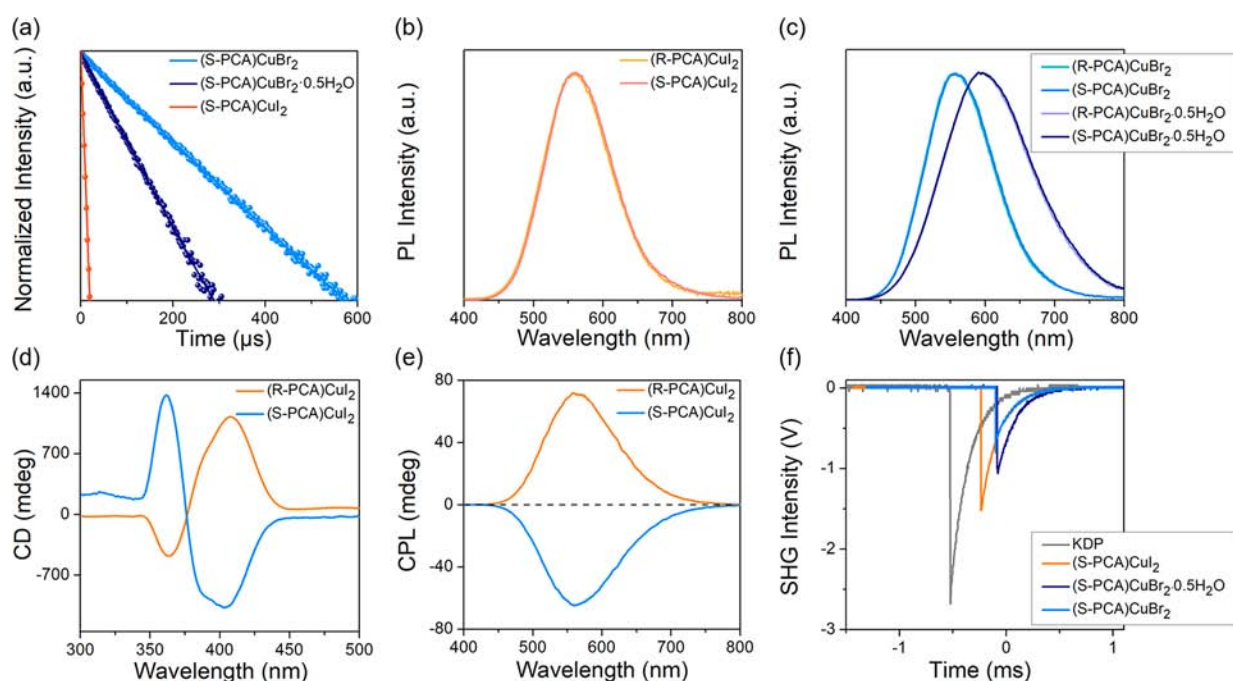


Figure 4. (a) Time-resolved PL decay spectra of (S-PCA)CuBr<sub>2</sub>, (S-PCA)CuBr<sub>2</sub>·0.5H<sub>2</sub>O, and (S-PCA)CuI<sub>2</sub> ( $\lambda_{\text{ex}} = 355$  nm). Steady-state PL spectra of (b) Cu(I)-based iodides and (c) Cu(I)-based bromides ( $\lambda_{\text{ex}} = 360$  nm). (d) CD spectra of (R,S-PCA)CuI<sub>2</sub>. (e) CPL spectra of polycrystalline (R,S-PCA)CuI<sub>2</sub>. (f) Comparison of the SHG responses of powdered (R,S-PCA)CuBr<sub>2</sub>, (S-PCA)CuBr<sub>2</sub>·0.5H<sub>2</sub>O, (R,S-PCA)CuI<sub>2</sub> and KDP under the particle size range (147–210  $\mu\text{m}$ ) at room temperature.

Table 1. Summary of the Properties of (S-PCA)CuBr<sub>2</sub>, (S-PCA)CuBr<sub>2</sub>·0.5H<sub>2</sub>O, and (S-PCA)CuI<sub>2</sub>

compound	(S-PCA)CuBr <sub>2</sub>	(S-PCA)CuBr <sub>2</sub> ·0.5H <sub>2</sub> O	(S-PCA)CuI <sub>2</sub>
space group	C2	C2	C2
absorption edge (eV)	2.87	3.66	2.70
PL emission (eV)	2.22	2.10	2.22
PLQY (F)	7.5	0.5	12.8
PL lifetime ( $\mu\text{s}$ )	123.9	62.4	4.3
CPL $g_{\text{lum}}$ ( $\times 10^{-3}$ )	-2.2	-2.1	-7.5

bands might be assigned to a triplet-cluster-centered (CC) excited state, which involves mixed iodide-to-metal charge transfer (XMCT) and metal-cluster-centered ( $d^{10}\text{Cu } d^9s^1\text{Cu}$ ) transitions.<sup>42,52–54</sup>

**CD and SHG.** CD spectra were collected at room temperature using single crystals of (R,S-PCA)CuI<sub>2</sub>. As shown in Figure 4d, mirrored CD signals appear at approximately 362 and 403 nm, which is in agreement with the absorption peaks (see Figure S4). The CD response stems from the Cotton effect of the [Cu<sub>4</sub>] absorption bands affected by the chiral (R,S-PCA) cations.<sup>55</sup> This result indicates that the chirality of [R,S-PCA]<sup>N</sup> has been efficiently transferred to the 2D framework, which is consistent with previously reported results.<sup>47,56</sup> Also noted the CD signals are overestimated due to the effects of linear dichroism and birefringence; what matters here are the opposite shape and peak positions.<sup>57,58</sup>

Combining the chiral structures and strong PL, we further explored the CPL properties of these Cu(I) halides. As shown in Figure 4b and e, the CPL emissions of (R,S-PCA)CuI<sub>2</sub> are consistent with the regular PL spectra regarding the emission width and the peak position. The CPL property can be evaluated according to the luminescence dissymmetry factors [ $g_{\text{lum}} = 2 \times (I_{\text{left}} - I_{\text{right}}) / (I_{\text{left}} + I_{\text{right}})$ ], where  $I_{\text{left}}$  and  $I_{\text{right}}$  refer

to the intensities of the left- and right-polarized emissions, respectively.<sup>59</sup> The  $g_{\text{lum}}$  values of (R,S-PCA)CuBr<sub>2</sub>, (R,S-PCA)CuBr<sub>2</sub>·0.5H<sub>2</sub>O, and (R,S-PCA)CuI<sub>2</sub> are  $2.1 \times 10^{-3}$  and  $-2.2 \times 10^{-3}$ ,  $3.7 \times 10^{-3}$  and  $-2.1 \times 10^{-3}$ , and  $8.3 \times 10^{-3}$  and  $-7.5 \times 10^{-3}$ , respectively, which are comparable to other Cu(I)-based chiral materials, (e.g., [D,L-valinol(18-crown-6)]<sup>N</sup>[Cu<sub>5</sub>(S<sup>t</sup>Bu)<sub>6</sub>]<sup>-</sup> ( $9.7 \times 10^{-3}$  and  $-9.7 \times 10^{-3}$ )<sup>60</sup> and (R,S-MBA)<sub>4</sub>Cu<sub>4</sub>I<sub>4</sub> ( $10.0 \times 10^{-3}$  and  $-6.0 \times 10^{-3}$ )<sup>61</sup> (see also Table S8). The absence of perfect mirror CPL spectra for these solid enantiomer powder samples could be due to aggregation inhomogeneity in the solid state.<sup>62,63</sup>

Because of the noncentrosymmetric nature of these materials, the SHG properties were also investigated. Using potassium dihydrogen phosphate (KDP) as the reference, SHG measurements were performed on polycrystalline powders under 1064 nm laser irradiation at ambient temperature. (S-PCA)CuBr<sub>2</sub>, (S-PCA)CuBr<sub>2</sub>·0.5H<sub>2</sub>O, and (S-PCA)CuI<sub>2</sub> exhibit nonlinear optical activities about 0.3 $\times$ , 0.4 $\times$ , and 0.6 $\times$  that of KDP, respectively (Figure 4f). The hydrated analogue shows a higher SHG intensity compared with the Cu–Br compound, which could be related to the change of the local Cu–Br–Cu bond angles. Among the compounds, (S-PCA)CuI<sub>2</sub> has the largest SHG response, likely due to the effect of the inherently smaller bandgap of the iodide.<sup>64</sup> Temperature-dependent SHG measurements were also carried out. For both compounds, higher temperatures lead to stronger SHG responses (Figure S8). Differential scanning calorimetry (DSC) analysis (Figure S9) indicates that (S-PCA)CuI<sub>2</sub> has no phase transition behavior within the range of 193–423 K. However, for (S-PCA)CuBr<sub>2</sub>, exothermic and endothermic peaks at 395 and 415 K can be observed in the cooling and warming modes, respectively, making it a potential candidate for stimuli-responsive SHG materials.<sup>65–68</sup>

**DFT Calculations.** In order to gain insights into the electronic structures of these Cu(I) halides and to better



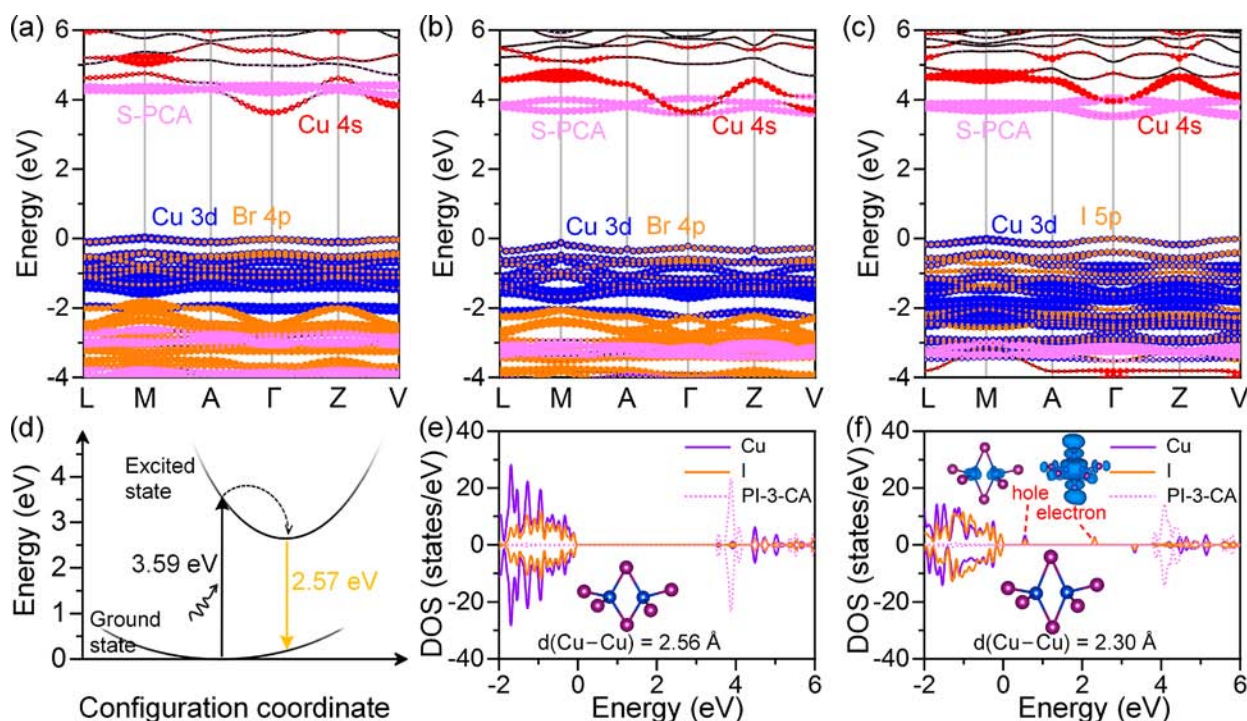


**Figure 5.** Calculated band structures for (a) (S-PCA)CuBr<sub>2</sub>, (b) (S-PCA)CuBr<sub>2</sub>·0.5H<sub>2</sub>O, and (c) (S-PCA)CuI<sub>2</sub>. (d) The configuration coordinate diagram illustrates the mechanism for the excitation, relaxation, and emission in (S-PCA)CuI<sub>2</sub>. Spin-polarized densities of states of (e) the ground state and (f) the STE state in (S-PCA)CuI<sub>2</sub>. The insets show the local structures and the charge density maps for the excited electron and hole.

understand of PL mechanism, DFT calculations were also carried out to calculate the electronic band structures. As shown in Figure 5, (S-PCA)CuBr<sub>2</sub> and (S-PCA)CuBr<sub>2</sub>·0.5H<sub>2</sub>O have slightly indirect bandgaps of 3.61 and 3.70 eV, respectively. For both compounds, the valence band CB is made up of Cu 4s orbitals, while for (S-PCA)CuBr<sub>2</sub>·0.5H<sub>2</sub>O the VBM consists of the Cu 3d and Br 4p orbitals and the CBM consists of the Cu 4s orbitals and molecular orbitals of S-PCA. (S-PCA)CuI<sub>2</sub> has a calculated direct bandgap of 3.51 eV, as the VBM and CBM are both located at the  $\Gamma$ -point. The VBM consists of the antibonding states of I 5p orbitals and Cu 3d, and the CBM is derived from the molecular orbitals of S-PCA. By and large, the calculated fundamental bandgap trend (3.61, 3.70, and 3.51 eV) is in agreement with the observed trend for the optical bandgaps (2.70, 3.66, and 2.87 eV) (Table S10). However, deviation exists as the determination of the exact fundamental bandgap for a low dimensional luminescent material is generally hindered by the existence of exciton absorption band, as often reported in literature.<sup>69,70,71</sup> As shown in Figure S12, for (S-PCA)CuBr<sub>2</sub>, the localized orbitals between carboxyl groups give rise to a smaller broadening of the band and a higher energy, resulting in Cu 4s orbitals being the CBM. For (S-PCA)CuBr<sub>2</sub>·0.5H<sub>2</sub>O, the delocalized orbitals between carboxyl groups increase the energy bandwidth and reduce the energy level positions, so the organic molecule contributes to the CBM. Similar to (S-PCA)CuBr<sub>2</sub>·0.5H<sub>2</sub>O, the carboxyl groups also contribute to the CBM in (S-PCA)CuI<sub>2</sub>. The stronger intermolecular interactions and the larger energy bandwidth are due to the short distance between carboxyl groups in (S-PCA)CuI<sub>2</sub>. Since the antibonding orbital composed of I 5p and Cu 3d orbitals has a relatively higher energy, the calculated bandgap is the smallest for (S-PCA)CuI<sub>2</sub>. The main reasons for the similar calculated fundamental bandgaps of these three halides are that the

VBM is contributed by the Cu 3d orbital and less affected by the halogen p orbitals, and that the CBM is derived mainly from the Cu 4s orbital or organic molecular orbitals with comparable energy levels.

In general, the PL emission of metal halides typically redshifts when changing from Br to I. However, the PL emission peaks of (R,S-PCA)CuBr<sub>2</sub> and (R,S-PCA)CuI<sub>2</sub> are almost identical, and only (R,S-PCA)CuBr<sub>2</sub>·0.5H<sub>2</sub>O shows a PL redshift. The excited-state calculations indicate that the observed emissions are attributed from the self-trapped excitons (STEs) in these compounds, and the calculated emission peaks are located at 2.58 eV (481.6 nm) for (S-PCA)CuBr<sub>2</sub>, 2.57 eV (482.3 nm) for (S-PCA)CuI<sub>2</sub> and 2.33 eV (533.1 nm) for (S-PCA)CuBr<sub>2</sub>·0.5H<sub>2</sub>O (Figure 5d, S16), explaining well the experimental observations. As shown in Figures 5e, Figures 5f, and S15, under the excited state, structural distortions are prominent in all compounds due to exciton localization. Taking (S-PCA)CuI<sub>2</sub> as an example, structural relaxation breaks one Cu–I bond in the singlet state, which is accompanied by a decrease in the Cu–Cu distance from 2.56 to 2.30 Å. The charge density for the hole state is mainly located on the two Cu atoms of Cu<sub>2</sub>I<sub>6</sub> dimer unit, while the charge density of the electron state is mostly located in the direction of the connection between the two I atoms (Figures 5f and S15).

## 2 CONCLUSION

In conclusion, three pairs of chiral Cu(I)-based hybrids [(R,S-PCA)CuBr<sub>2</sub>, (R,S-PCA)CuBr<sub>2</sub>·0.5H<sub>2</sub>O, and (R,S-PCA)CuI<sub>2</sub>] featuring a new type of chiral 2D layered structure have been reported for the first time. The unique structural type is supported by the strong hydrogen bonding interaction between the carboxylate groups on the R,S-PCA organic cations. Specifically, (R,S-PCA)CuBr<sub>2</sub> exhibits hydrochromic

properties that can be reversibly converted to the hydrated phase  $(R/S\text{-PCA})\text{CuBr}_2 \cdot 0.5\text{H}_2\text{O}$ . With the successful chirality transfer, all compounds exhibit chiroptical properties, such as CD, CPL emissions, and SHG responses, that stem from the noncentrosymmetric nature of the structures. DFT calculations demonstrate that the bromide and iodide compounds are indirect and direct semiconductors, respectively, with similar bandgaps. The broad-band PL emission and the emission peak position were further investigated through DFT, revealing different STE mechanisms for each compound. Our work opens up new opportunities for achieving multifunctionality in the all-in-one Cu(I)-based layered semiconductors and provides new design guidelines for functional optoelectronic materials.

## 2. METHODS

**Materials.** Cuprous bromide (99.5F), cuprous iodide (99F), and  $(R/S)$ -piperidine-3-carboxylic acid (97F) were purchased from Bide Pharmatech Ltd. and directly used without further treatment. Hydrogen bromide (AR, 40F), hydriodic acid (47.0F), and hypophosphorous acid (AR, 50 wt F in  $\text{H}_2\text{O}$ ) were purchased from Shanghai Macklin Biochemical Co., Ltd.

$(R/S\text{-PCA})\text{CuBr}_2$ . CuBr powder (0.430 g, 3 mmol) was dissolved in 2 mL of 40F aqueous HBr and 0.5 mL of 50F  $\text{H}_3\text{PO}_2$  by heating the mixture under stirring for 20 min at 124 °C until the solution turned colorless. Then, to the solution was slowly added 0.387 g (3 mmol) of  $(R/S)$ -piperidine-3-carboxylic acid under stirring. Colorless plate-like crystals precipitated as the reaction mixture slowly cooled to room temperature.

$(R/S\text{-PCA})\text{CuBr}_2 \cdot 0.5\text{H}_2\text{O}$ .  $(R/S\text{-PCA})\text{CuBr}_2 \cdot 0.5\text{H}_2\text{O}$  can be obtained by the above similar synthesis method by reducing the amount of the reactant to 2 mmol and increasing the amount of hydrobromic acid to 3 mL. Crystals formed in open containers while the solvent slowly evaporated. Alternatively, the phase with water can also be obtained by placing  $(R/S\text{-PCA})\text{CuBr}_2$  in the mother liquor for 2 weeks. Additionally,  $(R/S\text{-PCA})\text{CuBr}_2 \cdot 0.5\text{H}_2\text{O}$  can be converted to  $(R/S\text{-PCA})\text{CuBr}_2$  by vacuum drying the sample at 60 °C for 2 h.

$(R/S\text{-PCA})\text{CuI}_2$ .  $(R/S\text{-PCA})\text{CuI}_2$  can be obtained with a synthetic process similar to that for  $(R/S\text{-PCA})\text{CuBr}_2$ . CuI powder (0.381 g, 2 mmol) was dissolved in 4 mL of 40F aqueous HI and 1.0 mL of 50F  $\text{H}_3\text{PO}_2$  by heating the mixture under stirring for 10 min at 127 °C until the solution became clear. Then, to the solution was slowly added 0.258 g (2 mmol) of  $(R/S)$ -piperidine-3-carboxylic acid under stirring. Light yellow plate-like crystals precipitated as the mixture slowly cooled to room temperature.

**Structural Determinations.** The intensity data for single crystals of  $(R/S\text{-PCA})\text{CuBr}_2$ ,  $(R/S\text{-PCA})\text{CuBr}_2 \cdot 0.5\text{H}_2\text{O}$ , and  $(R/S\text{-PCA})\text{CuI}_2$  were collected on a Bruker APEX-II CCD diffractometer with Mo  $K\alpha$  radiation at room temperature. The collection and reduction of crystal data were carried out using a Bruker APEX3 instrument. The crystal structures were solved with SHELXT methods with the Olex2 program. All non-hydrogen atoms were refined anisotropically. Hydrogen atoms were placed at the geometric position. The details of the crystallographic data and selected bond parameters for these compounds are listed in Tables S1–S3.

**Steady-State and Time-Resolved Photoluminescence.** Steady-state PL spectra were recorded on a HORIBA FluoroMaxN instrument with a solid-state sample holder at room temperature. PLQYs were examined at room temperature using the integrating sphere on a Hamamatsu Photonics C11347–11 Quantaaurus-QY ( $\lambda_{\text{ex}} = 360$  nm) instrument. The PL decay curves were recorded at room temperature. The excitation source was a pulsed ultraviolet femosecond laser operated at 355 nm (Coherent Astrella ultrafast Ti:sapphire laser with OperA Solo, pulse width of 100 fs and repetition rate of 1 kHz). The signal was dispersed by a 320 mm monochromator (iHR320 from Horiba, Ltd.) with suitable filters and detected based on the time-correlated single-photon counting (TCSPC) technique.

**Optical Absorption Spectroscopy.** The solid LV–vis absorbance spectra were recorded at room temperature on a LV-3600i plus spectrophotometer with  $\text{BaSO}_4$  as the reference substance in the wavelength range of 200–900 nm.

**SHG Measurements.** Powder SHG measurements were performed using an Nd:YAG laser (1064 nm) with an input pulse of 350 mV on a modified Kurtz-NLO system.

**Circular Dichroism.** CD spectra for single-crystalline crystals were recorded on a CD spectrometer (Chirascan, Applied Photophysics). The wavelength and bandwidth of the monochromator were set to 280.0 and 1.0 nm, and the time-per-point of each sampling point was 0.5 s.

**Circularly Polarized Luminescence.** The CPL spectra were recorded on a CPL spectrometer (CPL-300, JASCO) in the solid state. The parameters for the CPL measurement were set as follows: scanning speed of 200 nm/min, D.I.T. of 2 s, bandwidth of 2000  $\mu\text{m}$ , and a number of accumulations higher than 7.

**Computational Details.** DFT calculations were performed in the Vienna Ab Initio Simulation Package (VASP) code using the projector-augmented wave (PAW) method.<sup>72</sup> To correct the van der Waals interactions, the DFT-D3 correction method of Grimme was employed.<sup>73,74</sup> The cutoff energy for the electron wave was set to 400 eV. All crystal structures were fully relaxed until the total force on each atom was 0.03 eV/Å. The Perdew–Burke–Ernzerhof (PBE) function was used as exchange–correlation functional for structural relaxation.<sup>75</sup> Centered k-meshes with a k-spacing of 0.2  $\text{Å}^{-1}$  were employed to sample the Brillouin zones. For the calculations of electronic properties, Heyd–Scuseria–Ernzerhof (HSE) hybrid functionals were used.<sup>76,77</sup> For excited-state calculations, supercells of up to 192 atoms for  $(S\text{-PCA})\text{CuBr}_2$  and  $(S\text{-PCA})\text{CuI}_2$  and 204 atoms for  $(S\text{-PCA})\text{CuBr}_2 \cdot 0.5\text{H}_2\text{O}$  ( $2 \times 2 \times 1$  primitive cells) were considered. The optimized ground- and excited-state structures were obtained using the HSE functional, and the atomic positions were fully relaxed until the residual forces were less than 0.03 eV/Å. The electrons and holes of these compounds are both strongly localized, so the self-consistent field (SCF) method can easily be used for the STEs. The SCF method combined with the HSE functional can allow the accurate calculation of excited-state structural relaxation, and the emission energy of a STE at an excited-state energy minimum can be calculated based on the relaxed exciton structure following the Franck–Condon principle.

## 2. SUPPORTING INFORMATION

### Supporting Information

The Supporting Information is available free of charge at <https://pubs.acs.org/doi/10.1021/acs.chemmater.2c01729>.

Additional characterization and calculation details (PDF)

$(R\text{-PCA})\text{CuBr}_2$  (CIF)

$(S\text{-PCA})\text{CuBr}_2$  (CIF)

$(R\text{-PCA})\text{CuBr}_2 \cdot \text{H}_2\text{O}$  (CIF)


$(S\text{-PCA})\text{CuBr}_2 \cdot \text{H}_2\text{O}$  (CIF)


$(R\text{-PCA})\text{CuI}_2$  (CIF)

$(S\text{-PCA})\text{CuI}_2$  (CIF)

## 2. AUTHOR INFORMATION


### Corresponding Authors

Zewen Xiao – Wuhan National Laboratory for Optoelectronics, Huazhong University of Science and Technology, Wuhan, Hubei 430074, China  [orcid.org/0000-0002-4911-1399](https://orcid.org/0000-0002-4911-1399); Email: [zwxiao@hust.edu.cn](mailto:zwxiao@hust.edu.cn)


Lingling Mao – Department of Chemistry, Southern University of Science and Technology, Shenzhen, Guangdong 518055, China  [orcid.org/0000-0003-3166-8559](https://orcid.org/0000-0003-3166-8559); Email: [maoll@sustech.edu.cn](mailto:maoll@sustech.edu.cn)



## ✉ authors

**Xiaoqin Ji** – Department of Chemistry, Southern University of Science and Technology, Shenzhen, Guangdong 518055, China  [orcid.org/0000-0002-8220-9005](https://orcid.org/0000-0002-8220-9005)


**Shining Geng** – Wuhan National Laboratory for Optoelectronics, Huazhong University of Science and Technology, Wuhan, Hubei 430074, China

**Shuai Zhang** – State Key Laboratory of Luminescent Materials and Devices, Guangdong Provincial Key Laboratory of Fiber Laser Materials and Applied Technologies, South China University of Technology, Guangzhou, Guangdong 510641, China  [orcid.org/0000-0001-9723-9832](https://orcid.org/0000-0001-9723-9832)


**Yaping Gong** – MOE Key Laboratory of Bioinorganic and Synthetic Chemistry, School of Chemistry, Sun Yat-sen University, Guangzhou, Guangdong 510275, China

**Xuanyu Zhang** – Department of Electrical and Electronic Engineering, Southern University of Science and Technology, Shenzhen, Guangdong 518055, China

**Ruiqian Li** – Department of Chemistry, Southern University of Science and Technology, Shenzhen, Guangdong 518055, China

**Yang Liu** – Department of Chemistry, Southern University of Science and Technology, Shenzhen, Guangdong 518055, China  [orcid.org/0000-0002-2189-4774](https://orcid.org/0000-0002-2189-4774)

**Jian Chen** – Department of Chemistry, Southern University of Science and Technology, Shenzhen, Guangdong 518055, China

**Rui Chen** – Department of Electrical and Electronic Engineering, Southern University of Science and Technology, Shenzhen, Guangdong 518055, China  [orcid.org/0000-0002-0445-7847](https://orcid.org/0000-0002-0445-7847)

Complete contact information is available at:

<https://pubs.acs.org/doi/10.1021/acs.chemmater.2c01729>

## Notes

The authors declare no competing financial interest. CCDC 2175971, 2175974–2175978 contain the supplementary crystallographic data for this paper. These data can be obtained free of charge from The Cambridge Crystallographic Data Centre.

## ACKNOWLEDGMENTS

This work was supported by a SLSTech startup grant (Y01216150). The authors are grateful for the assistance of SLSTech Core Research Facilities. We thank Prof. Shi Ye and Prof. Wei-Xiong Zhang for their help with the characterizations.

## REFERENCES

- (1) Li, W.; Wang, Z.; Deschler, F.; Gao, S.; Friend, R. H.; Cheetham, A. K. Chemically diverse and multifunctional hybrid organic–inorganic perovskites. *Nat. Rev. Mater.* **2017**, *2*, 16099.
- (2) Milic, J. V. Multifunctional layered hybrid perovskites. *J. Mater. Chem. C* **2021**, *9*, 11428–11443.
- (3) Coronado, E.; Forment-Aliaga, A.; Galvín-Mascaró, J. R.; Giménez-Saiz, C.; Gómez-García, C. J.; Martín-Ferrero, E.; Nuez, A.; Romero, F. M. Multifunctional molecular materials. *Solid State Sci.* **2003**, *5*, 917–924.
- (4) Kirchon, A.; Feng, L.; Drake, H. F.; Joseph, E. A.; Zhou, H.-C. From fundamentals to applications: a toolbox for robust and multifunctional MOF materials. *Chem. Soc. Rev.* **2011**, *47*, 8611–8638.

(5) Lin, R.-B.; Xiang, S.; Li, B.; Cui, Y.; Qian, G.; Zhou, W.; Chen, B. Our journey of developing multifunctional metal-organic frameworks. *Coord. Chem. Rev.* **2019**, *384*, 21–36.

(6) Train, C.; Gheorghe, R.; Krstic, V.; Chamoiseau, L.-M.; Ovanessian, N. S.; Rikken, G. L. J. A.; Gruselle, M.; Verdager, M. Strong magneto-chiral dichroism in enantiopure chiral ferromagnets. *Nat. Mater.* **2001**, *7*, 729–734.

(7) Lochenie, C.; Schütz, K.; Panzer, F.; Kurz, H.; Maier, B.; Puchtler, F.; Agarwal, S.; KZähler, A.; Weber, B. Spin-Crossover Iron(II) Coordination Polymer with Fluorescent Properties: Correlation between Emission Properties and Spin State. *J. Am. Chem. Soc.* **2011**, *143*, 700–709.

(8) Qin, C.; Sandanayaka, A. S. D.; Zhao, C.; Matsushima, T.; Zhang, D.; Fukushima, T.; Adachi, C. Stable room-temperature continuous-wave lasing in quasi-2D perovskite films. *Nature* **2020**, *585*, 53–57.

(9) Lin, Y.-H.; Sakai, N.; Da, P.; Wu, J.; Sansom, H. C.; Ramadan, A. J.; Mahesh, S.; Liu, J.; Oliver, R. D. J.; Lim, J.; Aspirtarte, L.; Sharma, K.; Madhu, P. K.; Morales-Vilches, A. B.; Nayak, P. K.; Bai, S.; Gao, F.; Grovenor, C. R. M.; Johnston, M. B.; Labram, J. G.; Durrant, J. R.; Ball, J. M.; Wenger, B.; Stannowski, B.; Snaith, H. J. A piperidinium salt stabilizes efficient metal-halide perovskite solar cells. *Science* **2020**, *369*, 96–102.

(10) Chung, I.; Lee, B.; He, J.; Chang, R. P. H.; Kanatzidis, M. G. All-solid-state dye-sensitized solar cells with high efficiency. *Nature* **2012**, *485*, 486–489.

(11) Ahmadi, M.; Wu, T.; Hu, B. A Review on Organic–Inorganic Halide Perovskite Photodetectors: Device Engineering and Fundamental Physics. *Adv. Mater.* **2017**, *29*, 1605242.

(12) Mao, L.; Stoumpos, C. C.; Kanatzidis, M. G. Two-Dimensional Hybrid Halide Perovskites: Principles and Promises. *J. Am. Chem. Soc.* **2019**, *141*, 1171–1190.

(13) Smith, M. D.; Crace, E. J.; Jaffe, A.; Karunadasa, H. I. The Diversity of Layered Halide Perovskites. *Annu. Rev. Mater. Res.* **2011**, *48*, 111–136.

(14) Mao, L.; Chen, J.; Vishnoi, P.; Cheetham, A. K. The Renaissance of Functional Hybrid Transition-Metal Halides. *Acc. Mater. Res.* **2022**, *3*, 439–448.

(15) Long, G.; Sabatini, R.; Saidaminov, M. I.; Lakhwani, G.; Rasmita, A.; Liu, X.; Sargent, E. H.; Gao, W. Chiral-perovskite optoelectronics. *Nat. Rev. Mater.* **2020**, *5*, 423–439.

(16) Jana, M. K.; Song, R.; Liu, H.; Khanal, D. R.; Janke, S. M.; Zhao, R.; Liu, C.; Vally Vardeny, Z.; Blum, V.; Mitzi, D. B. Organic-to-inorganic structural chirality transfer in a 2D hybrid perovskite and impact on Rashba-Dresselhaus spin-orbit coupling. *Nat. Commun.* **2020**, *11*, 4699.

(17) Long, G.; Jiang, C.; Sabatini, R.; Yang, Z.; Wei, M.; Quan, L. N.; Liang, Q.; Rasmita, A.; Askerka, M.; Walters, G.; Gong, X.; Xing, J.; Wen, X.; Quintero-Bermudez, R.; Yuan, H.; Xing, G.; Wang, X. R.; Song, D.; Voznyy, O.; Zhang, M.; Hoogland, S.; Gao, W.; Xiong, Q.; Sargent, E. H. Spin control in reduced-dimensional chiral perovskites. *Nat. Photonics* **2011**, *12*, 528–533.

(18) Lu, H.; Xiao, C.; Song, R.; Li, T.; Maughan, A. E.; Levin, A.; Brunecky, R.; Berry, J. J.; Mitzi, D. B.; Blum, V.; Beard, M. C. Highly Distorted Chiral Two-Dimensional Tin Iodide Perovskites for Spin Polarized Charge Transport. *J. Am. Chem. Soc.* **2020**, *142*, 13030–13040.

(19) Dong, Y.; Zhang, Y.; Li, X.; Feng, Y.; Zhang, H.; Xu, J. Chiral Perovskites: Promising Materials toward Next-Generation Optoelectronics. *Small* **2019**, *15*, 1902237.

(20) Ostovar pour, S.; Rocks, L.; Faulds, K.; Graham, D.; Parchansky, V.; Bour, P.; Blanch, E. W. Through-space transfer of chiral information mediated by a plasmonic nanomaterial. *Nat. Chem.* **2017**, *7*, 591–596.

(21) Mušca, V. Chirality transfer takes a Sump. *Nat. Chem.* **2017**, *7*, 543–544.

(22) Ahn, J.; Lee, E.; Tan, J.; Yang, W.; Kim, B.; Moon, J. A new class of chiral semiconductors: chiral-organic-molecule-incorporating

- organic–inorganic hybrid perovskites. *Mater. Horiz.* **2017**, *4*, 851–856.
- (23) Qin, Y.; Gao, F.-F.; Qian, S.; Guo, T.-M.; Gong, Y.-J.; Li, Z.-G.; Su, G.-D.; Gao, Y.; Li, W.; Jiang, C.; Lu, P.; Bu, X.-H. Multifunctional Chiral 2D Lead Halide Perovskites with Circularly Polarized Photoluminescence and Piezoelectric Energy Harvesting Properties. *ACS Nano* **2022**, *16*, 3221–3230.
- (24) Yuan, C.; Li, X.; Semin, S.; Feng, Y.; Rasing, T.; Xu, J. Chiral Lead Halide Perovskite Nanowires for Second-Order Nonlinear Optics. *Nano Lett.* **2011**, *18*, 5411–5417.
- (25) Naciri, J.; Shenoy, D. K.; Keller, P.; Gray, S.; Crandall, K.; Shashidhar, R. Synthesis and Pyroelectric Properties of Novel Ferroelectric Organosiloxane Liquid Crystalline Materials. *Chem. Mater.* **2002**, *14*, 5134–5139.
- (26) Yang, C.-K.; Chen, W.-N.; Ding, Y.-T.; Wang, J.; Rao, Y.; Liao, W.-Q.; Tang, Y.-Y.; Li, P.-F.; Wang, Z.-X.; Xiong, R.-G. The First 2D Homochiral Lead Iodide Perovskite Ferroelectrics: [R- and S-1-(4-Chlorophenyl)ethylammonium]<sub>2</sub>PbI<sub>4</sub>. *Adv. Mater.* **2019**, *31*, 1808088.
- (27) Zhang, H.-Y.; Tang, Y.-Y.; Shi, P.-P.; Xiong, R.-G. Toward the Targeted Design of Molecular Ferroelectrics: Modifying Molecular Symmetries and Homochirality. *Acc. Chem. Res.* **2019**, *52*, 1928–1938.
- (28) Lu, H.; Wang, J.; Xiao, C.; Pan, X.; Chen, X.; Brunecy, R.; Berry, J. J.; Zhu, K.; Beard, M. C.; Vardeny, Z. V. Spin-dependent charge transport through 2D chiral hybrid lead-iodide perovskites. *Sci. Adv.* **2019**, *5*, eaay0571.
- (29) Lu, Y.; Wang, Q.; Chen, R.; Qiao, L.; Zhou, F.; Yang, X.; Wang, D.; Cao, H.; He, W.; Pan, F.; Yang, Z.; Song, C. Spin-Dependent Charge Transport in 1D Chiral Hybrid Lead-Bromide Perovskite with High Stability. *Adv. Funct. Mater.* **2021**, *31*, 2104605.
- (30) Wang, B.; Wang, C.; Chu, Y.; Zhang, H.; Sun, M.; Wang, H.; Wang, S.; Zhao, G. Environmental-friendly lead-free chiral Mn-based metal halides with efficient circularly polarized photoluminescence at room temperature. *J. Alloy. Compd.* **2022**, *918*, 164892.
- (31) Chen, J.; Zhang, S.; Pan, X.; Li, R.; Ye, S.; Cheetham, A. K.; Mao, L. Structural Origin of Enhanced Circularly Polarized Luminescence in Hybrid Manganese Bromides. *Angew. Chem. Int. Ed.* **2022**, *61* (30), e202205906.
- (32) Mande, H. M.; Ghalsasi, P. S.; Arulsamy, N. Racemic and conglomerate 1-(4-haloaryl)ethylammonium tetrachlorocobaltate salts: formation of helical structures. *RSC Adv.* **2011**, *5*, 62719–62723.
- (33) Tang, Y.-Y.; Ai, Y.; Liao, W.-Q.; Li, P.-F.; Wang, Z.-X.; Xiong, R.-G. H<sub>2</sub>F-Substitution-Induced Homochirality for Designing High-Tc Molecular Perovskite Ferroelectrics. *Adv. Mater.* **2019**, *31*, 1902163.
- (34) Li, L.-S.; Tan, Y.-H.; Wei, W.-J.; Gao, H.-Q.; Tang, Y.-Z.; Han, X.-B. Chiral Switchable Low-Dimensional Perovskite Ferroelectrics. *ACS Appl. Mater. Interfaces* **2021**, *13*, 2044–2051.
- (35) Zhao, L.; Han, X.; Zheng, Y.; Yu, M.-H.; Xu, J. Tin-Based Chiral Perovskites with Second-Order Nonlinear Optical Properties. *Adv. Photonics Res.* **2021**, *2*, 2100056.
- (36) Dehnhardt, N.; Axt, M.; Zimmermann, J.; Yang, M.; Mette, G.; Heine, J. Band Gap-Tunable, Chiral Hybrid Metal Halides Displaying Second-Harmonic Generation. *Chem. Mater.* **2020**, *32*, 4801–4807.
- (37) Moon, T. H.; Oh, S.-J.; Ok, K. M. [((R)-C<sub>8</sub>H<sub>12</sub>N)<sub>4</sub>][Bi<sub>2</sub>Br<sub>10</sub>] and [((S)-C<sub>8</sub>H<sub>12</sub>N)<sub>4</sub>][Bi<sub>2</sub>Br<sub>10</sub>]: Chiral Hybrid Bismuth Bromides Templated by Chiral Organic Cations. *ACS Omega* **2011**, *3*, 17895–17903.
- (38) Yao, L.; Zeng, Z.; Cai, C.; Xu, P.; Gu, H.; Gao, L.; Han, J.; Zhang, X.; Wang, X.; Wang, X.; Pan, A.; Wang, J.; Liang, W.; Liu, S.; Chen, C.; Tang, J. Strong Second- and Third-Harmonic Generation in 1D Chiral Hybrid Bismuth Halides. *J. Am. Chem. Soc.* **2021**, *143*, 16095–16104.
- (39) Hao, J.; Lu, H.; Mao, L.; Chen, X.; Beard, M. C.; Blackburn, J. L. Direct Detection of Circularly Polarized Light Using Chiral Copper Chloride–Carbon Nanotube Heterostructures. *ACS Nano* **2021**, *15*, 7608–7617.
- (40) Lu, Y.; Wang, Q.; He, R.; Zhou, F.; Yang, X.; Wang, D.; Cao, H.; He, W.; Pan, F.; Yang, Z.; Song, C. Highly Efficient Spin-Filtering Transport in Chiral Hybrid Copper Halides. *Angew. Chem., Int. Ed.* **2021**, *60*, 23578–23583.
- (41) Peng, R.; Li, M.; Li, D. Copper(I) halides: A versatile family in coordination chemistry and crystal engineering. *Coord. Chem. Rev.* **2010**, *254*, 1–18.
- (42) Liu, W.; Fang, Y.; Li, J. Copper Iodide Based Hybrid Phosphors for Energy-Efficient General Lighting Technologies. *Adv. Funct. Mater.* **2011**, *28*, 1705593.
- (43) Benito, Q.; Le Goff, X. F.; Maron, S.; Fargues, A.; Garcia, A.; Martineau, C.; Taulelle, F.; Kahlal, S.; Gacoin, T.; Boilot, J.-P.; Perruchas, S. Polymorphic Copper Iodide Clusters: Insights into the Mechanochromic Luminescence Properties. *J. Am. Chem. Soc.* **2011**, *136*, 11311–11320.
- (44) Deng, M.; Mukthar, N. F. M.; Schley, N. D.; Lng, G. Yellow Circularly Polarized Luminescence from C<sub>1</sub>-Symmetrical Copper(I) Complexes. *Angew. Chem., Int. Ed.* **2020**, *59*, 1228–1231.
- (45) Zhang, M.-M.; Dong, X.-Y.; Wang, Z.-Y.; Li, H.-Y.; Li, S.-J.; Zhao, X.; Zang, S.-Q. AIE Triggers the Circularly Polarized Luminescence of Atomically Precise Enantiomeric Copper(I) Alkynyl Clusters. *Angew. Chem., Int. Ed.* **2020**, *59*, 10052–10058.
- (46) Wang, J.-J.; Zhou, H.-T.; Yang, J.-N.; Feng, L.-Z.; Yao, J.-S.; Song, K.-H.; Zhou, M.-M.; Jin, S.; Zhang, G.; Yao, H.-B. Chiral Phosphine–Copper Iodide Hybrid Cluster Assemblies for Circularly Polarized Luminescence. *J. Am. Chem. Soc.* **2021**, *143*, 10860–10864.
- (47) Ge, F.; Li, B.-H.; Cheng, P.; Li, G.; Ren, Z.; Xu, J.; Bu, X.-H. Chiral Hybrid Copper(I) Halides for High Efficiency Second Harmonic Generation with a Broadband Transparency Window. *Angew. Chem., Int. Ed.* **2022**, *61* (10), e202115024.
- (48) Yue, C.-Y.; Lin, N.; Gao, L.; Jin, Y.-X.; Liu, Z.-Y.; Cao, Y.-Y.; Han, S.-S.; Lian, X.-K.; Hu, B.; Lei, X.-W. Organic cation directed one-dimensional cuprous halide compounds: syntheses, crystal structures and photoluminescence properties. *Nat. Commun.* **2019**, *10*, 10151–10159.
- (49) Garc a-Fern andez, A.; Marcos-Cives, I.; Platas-Iglesias, C.; Castro-Garc a, S.; V azquez-Garc a, D.; Fern andez, A.; S anchez-Andu sar, M. Diimidazolium Halobismuthates [Dim]<sub>2</sub>[Bi<sub>2</sub>X<sub>10</sub>] (X = Cl<sup>−</sup>, Br<sup>−</sup>, or I<sup>−</sup>): A New Class of Thermochromic and Photoluminescent Materials. *Inorg. Chem.* **2011**, *57*, 7655–7664.
- (50) Xu, L.-J.; Plaviak, A.; Lin, X.; Worku, M.; He, Q.; Chaaban, M.; Kim, B. J.; Ma, B. Metal Halide Regulated Photophysical Tuning of Zero-Dimensional Organic Metal Halide Hybrids: From Efficient Phosphorescence to Long Afterglow. *Angew. Chem., Int. Ed.* **2020**, *59*, 23067–23071.
- (51) Berezin, A. S.; Davydova, M. P.; Samsonenko, D. G.; Sukhikh, T. S.; Artemev, A. V. A family of brightly emissive homo- and mixed-halomanganates(II): The effect of halide on optical and magnetic properties. *J. Lumin.* **2021**, *236*, 118069.
- (52) Yam, V. W.-W.; Au, V. K.-M.; Leung, S. Y.-L. Light-Emitting Self-Assembled Materials Based on d8 and d10 Transition Metal Complexes. *Chem. Rev.* **2011**, *115*, 7589–7728.
- (53) Li, S.-L.; Zhang, F.-Q.; Zhang, X.-M. An organic-ligand-free thermochromic luminescent cuprous iodide trinuclear cluster: evidence for cluster centered emission and configuration distortion with temperature. *Chem. Commun.* **2011**, *51*, 8062–8065.
- (54) Kyle, K. R.; DiBenedetto, J.; Ford, P. C. Dual photoemissions from the room temperature solutions of the tetranuclear copper(I) clusters Cu<sub>4</sub>I<sub>4</sub>(py-X)<sub>4</sub>(py-X = substituted pyridine). *J. Chem. Soc., Chem. Commun.* **1919**, 714–715.
- (55) Schellman, J. A.; Oriol, P. Origin of the Cotton Effect of Helical Polypeptides. *J. Chem. Phys.* **1962**, *37*, 2114–2124.
- (56) Guo, Z.; Li, J.; Wang, C.; Liu, R.; Liang, J.; Gao, Y.; Cheng, J.; Zhang, W.; Zhu, X.; Pan, R.; He, T. Giant Optical Activity and Second Harmonic Generation in 2D Hybrid Copper Halides. *Angew. Chem., Int. Ed.* **2021**, *60*, 8441–8445.
- (57) Dang, Y.; Liu, X.; Sun, Y.; Song, J.; Hu, W.; Tao, X. Bulk Chiral Halide Perovskite Crystals for Active Circular Dichroism and



Circularly Polarized Luminescence. *J. Phys. Chem. Lett.* **2020**, *11*, 1689–1696.

(58) Bilotti, I.; Biscarini, P.; Castiglioni, E.; Ferranti, F.; Kuroda, R. Reflectance circular dichroism of solid-state chiral coordination compounds. *Chirality* **2002**, *14*, 750–756.

(59) Richardson, F. S.; Riehl, J. P. Circularly polarized luminescence spectroscopy. *Chem. Rev.* **1977**, *77*, 773–792.

(60) Jin, Y.; Li, S.; Han, Z.; Yan, B.-J.; Li, H.-Y.; Dong, X.-Y.; Zang, S.-Q. Cations Controlling the Chiral Assembly of Luminescent Atomically Precise Copper(I) Clusters. *Angew. Chem., Int. Ed.* **2019**, *58*, 12143–12148.

(61) Yao, L.; Niu, G.; Li, J.; Gao, L.; Luo, X.; Xia, B.; Liu, Y.; Du, P.; Li, D.; Chen, C.; Zheng, Y.; Xiao, Z.; Tang, J. Circularly Polarized Luminescence from Chiral Tetranuclear Copper(I) Iodide Clusters. *J. Phys. Chem. Lett.* **2020**, *11*, 1255–1260.

(62) Li, B.; Li, Y.; Chan, M. H.-Y.; Yam, V. W.-W. Phosphorescent Cyclometalated Platinum(II) Enantiomers with Circularly Polarized Luminescence Properties and Their Assembly Behaviors. *J. Am. Chem. Soc.* **2021**, *143*, 21676–21684.

(63) Pan, X.; Zheng, A.; Yu, X.; Di, Q.; Li, L.; Duan, P.; Ye, K.; Naumov, P.; Zhang, H. A Low-Temperature-Resistant Flexible Organic Crystal with Circularly Polarized Luminescence. *Angew. Chem., Int. Ed.* **2022**, *61* (25), e202203938.

(64) Huang, L.-y.; Lambrecht, W. R. L. Vibrational spectra and nonlinear optical coefficients of rhombohedral CsGeX<sub>3</sub> halide compounds with X = I, Br, Cl. *Phys. Rev. B* **2016**, *94*, 115202.

(65) Wu, K.; Yang, Y.; Gao, L. A review on phase transition and structure-performance relationship of second-order nonlinear optical polymorphs. *Coord. Chem. Rev.* **2020**, *418*, 213380.

(66) Liu, S.; He, L.; Wang, Y.; Shi, P.; Ye, Q. Tunable phase transition, band gap and SHG properties by halogen replacement of hybrid perovskites [(thiomorpholinium)PbX<sub>3</sub>, X = Cl, Br, I]. *Chin. Chem. Lett.* **2022**, *33*, 1032–1036.

(67) Zeng, Y.; Hu, C. L.; Xu, W. J.; Zeng, T. W.; Zhu, Z. X.; Chen, X. X.; Liu, D. X.; Chen, Y. J.; Zhang, Y. B.; Zhang, W. X.; Chen, X. M. An Exceptional Thermally Induced Four-State Nonlinear Optical Switch Arising from Stepwise Molecular Dynamic Changes in a New Hybrid Salt. *Angew. Chem., Int. Ed.* **2022**, *61*, e202110082.

(68) Xiong, R.-G.; Lu, S.-Q.; Zhang, Z.-X.; Cheng, H.; Li, P.-F.; Liao, W.-Q. A Chiral Thermochromic Ferroelastic with Seven Physical Channel Switches. *Angew. Chem., Int. Ed.* **2020**, *59*, 9574–9578.

(69) Wang, S.; Morgan, E. E.; Panuganti, S.; Mao, L.; Vishnoi, P.; Wu, G.; Liu, Q.; Kanatzidis, M. G.; Schaller, R. D.; Seshadri, R. Ligand Control of Structural Diversity in Luminescent Hybrid Copper(I) Iodides. *Chem. Mater.* **2022**, *34*, 3206–3216.

(70) Wu, R. Red-Emitting Perovskite Variant Cs<sub>2</sub>PtCl<sub>6</sub> Phosphor: Material Design, Luminous Mechanism, and Application in High-Color-Rendering White Light-Emitting Diodes. *Adv. Opt. Mater.* **2022**, 2201081.

(71) Tan, Z.; Chu, Y.; Chen, J.; Li, J.; Ji, G.; Niu, G.; Gao, L.; Xiao, Z.; Tang, J. Lead-Free Perovskite Variant Solid Solutions Cs<sub>2</sub>Sn<sub>1-x</sub>Ta<sub>x</sub>Cl<sub>6</sub>: Bright Luminescence and High Anti-Water Stability. *Adv. Mater.* **2020**, *32*, 2002443.

(72) Kresse, G.; Furthmüller, J. Efficient iterative schemes for ab initio total-energy calculations using a plane-wave basis set. *Phys. Rev. B* **1996**, *54*, 11169–11186.

(73) Grimme, S.; Antony, J.; Ehrlich, S.; Krieg, H. A consistent and accurate ab initio parametrization of density functional dispersion correction (DFT-D) for the 94 elements H-Pu. *J. Chem. Phys.* **2010**, *132*, 154104.

(74) Grimme, S.; Ehrlich, S.; Goerigk, L. Effect of the damping function in dispersion corrected density functional theory. *J. Comput. Chem.* **2011**, *32*, 1456–1465.

(75) Perdew, J. P.; Burke, K.; Ernzerhof, M. Generalized Gradient Approximation Made Simple. *Phys. Rev. Lett.* **1996**, *77*, 3865–3868.

(76) Heyd, J.; Scuseria, G. E.; Ernzerhof, M. Hybrid functionals based on a screened Coulomb potential. *J. Chem. Phys.* **2003**, *118*, 8207–8215.

(77) Heyd, J.; Scuseria, G. E.; Ernzerhof, M. Erratum: “Hybrid functionals based on a screened Coulomb potential” [*J. Chem. Phys.* **118**, 8207 (2003)]. *J. Chem. Phys.* **2006**, *124*, 219906.

## Recommended by ACS

### Induction of Chiral Hybrid Metal Halides from Achiral Building Blocks

Yongshen Zheng, Xian-He Bu, *et al.*

SEPTEMBER 05, 2022

JOURNAL OF THE AMERICAN CHEMICAL SOCIETY

READ 

### Dimensional Control of Chiral Antimony Halide Compounds for Enhanced Circular Dichroism

Li Yao, Jiang Tang, *et al.*

AUGUST 09, 2022

CRYSTAL GROWTH & DESIGN

READ 

### Enantiomeric Hydrogen-bonded Chains Driving Ferroelectric and Nonlinear Optical Behavior

Nan Zhang, Han-Yue Zhang, *et al.*

AUGUST 30, 2022

CHEMISTRY OF MATERIALS

READ 

### Optically Induced Long-Lived Chirality Memory in the Color-Tunable Chiral Lead-Free Semiconductor (R)/(S)-CHEA<sub>4</sub>Bi<sub>2</sub>Br<sub>x</sub>I<sub>10-x</sub> (x = 0–10)

Shangpu Liu, Felix Deschler, *et al.*

JULY 27, 2022

JOURNAL OF THE AMERICAN CHEMICAL SOCIETY

READ 

Get More Suggestions >